Smart Agricultural Technology 6 (2023) 100344

Contents lists available at ScienceDirect

Smart Agricultural Technology

journal homepage: www.journals.elsevier.com/smart-agricultural-technology

An analysis of the effects of water regime on grapevine canopy status using a UAV and a mobile robot

Diego Tiozzo Fasiolo [a], Alessandro Pichierri [b,c], Paolo Sivilotti [c], Lorenzo Scalera [a,*]

[a] Polytechnic Department of Engineering and Architecture, University of Udine, Via delle Scienze 206, Udine, 33100, Italy
[b] Department of Life Sciences, University of Trieste, Via Licio Giorgieri 5, Trieste, 34127, Italy
[c] Department of Food, Environmental, and Animal Sciences, University of Udine, Via delle Scienze 206, Udine, 33100, Italy

ARTICLE INFO

Editor: Spyros Fountas

Keywords:
Precision viticulture
Robotics
Water potential
Vegetation indexes
3D reconstruction

ABSTRACT

In this paper, we propose a novel approach for analyzing the effects of water regime on grapevine canopy status using robotics as an aid for monitoring and mapping. Data from an unmanned aerial vehicle (UAV) and a ground mobile robot are used to obtain multispectral images and multiple vegetation indexes, and the 3D reconstruction of the canopy, respectively. Unlike previous works, sixty vegetation indexes are computed precisely by using the projected area of the vineyard point cloud as a mask. Extensive experimental tests on repeated plots of Pinot gris vines show that the GDVI, PVI, and TGI vegetation indexes are positively correlated with the water potential: GDVI ($R^2 = 0.90$ and 0.57 for the stem and pre-dawn water potential, respectively), PVI ($R^2 = 0.90$ and 0.57), TGI ($R^2 = 0.87$ and 0.77). Furthermore, the canopy volume and the canopy area projected on the ground are impacted by the water status, as well as stem and pre-dawn water potential measurements. The results obtained in this work demonstrate the feasibility of the proposed approach and the potential of robotic technologies, supporting precision viticulture.

Nomenclature

Symbols

α^*	Critical radius of the Alpha Shape algorithm [m]
Ψ_{pd}	Pre-dawn water potential [MPa]
Ψ_{stem}	Stem water potential [MPa]
I	Vineyard raster image
V	Vineyard plot pixels set

Abbreviations

2GRBi	2 Green Red Blue index
B	Blue band
CSF	Cloth Simulation Filter
DAFB	Days After Full Bloom
DVI	Difference Vegetation Index
EVI2	Enhanced Vegetation Index 2
G	Green band
GDVI	Green Difference Vegetation Index
GNSS	Global Navigation Satellite System
IMU	Inertial Measurement Unit
LiDAR	Light Detection and Ranging
MCARI1	Modified Chlorophyll Absorption in Reflectance Index 1
MRVI	Modified Ratio Vegetation Index
MS	Medium Stress
MTVI1	Modified Triangular Vegetation Index 1
NDRE	Normalized Difference Red Edge
NDVI	Normalized Difference Vegetation Index
NIR	Near Infra-Red
PCA	Principal Component Analysis
PVI	Perpendicular Vegetation Index
R	Red band
RGB	Red Green Blue
ROS	Robot Operating System
RTKV	Real-Time Kinematics
SfM	Structure from Motion
SLAM	Simultaneous Localization and Mapping
SOR	Statistical Outlier Removal
SS	Severe Stress
TGI	Triangular Greenness Index
UAV	Unmanned Aerial Vehicle

* Corresponding author.
E-mail address: lorenzo.scalera@uniud.it (L. Scalera).

https://doi.org/10.1016/j.atech.2023.100344
Received 1 August 2023; Received in revised form 10 October 2023; Accepted 15 October 2023
Available online 20 October 2023

VI Vegetation Index
WW Well Watered

1. Introduction

Recently, due to global warming, drought has become a growing concern in the agricultural sector, threatening plant survival and world food supply [25]. Over the next few years, extreme drought events are projected to become more frequent, as it is testified by the Intergovernmental Panel on Climate Change of the United Nations [2]. Moreover, climate change-related rising temperatures will directly affect the evapotranspirative demand of plants and soil, increasing the risk of water stress for many crops [55]. At the same time, food demand is predicted to increase as the world's population grows, and the low water availability will negatively impact the food supply [24].

Plants have developed different strategies to cope with water stress [3]. Plants typically reduce their growth and close their stomata to mitigate water loss caused by transpiration with negative consequences on the photosynthesis rate [8]. The reduction in aerial growth caused by water stress depends on the reduced number and size of leaves resulting in a decrease in leaf area and plant canopy volume [53]. In some cases, inducing moderate water stress in plants can be useful to enhance drought tolerance, yield production, and physiological responses [49]. However, in case of severe water stress, the viability of plants may be threatened by the reduction of reserve substances and hydraulic failure [33].

The plant water status can be assessed using a variety of measurements, with water potential being considered the most reliable among the traditional methods. Unfortunately, the water potential is a destructive measurement, requires numerous samples per plot, and narrow working windows (usually between 12 noon and 3 p.m., or before dawn) [40]. Different measures of water potential are used for different purposes. For instance, the stem water potential is often used to detect water stress [16], whereas the pre-dawn water potential is used as a proxy for soil potential [31].

Other measurements, such as stomatal conductance, are even more complex due to the instrumentation and calibration required [40]. Moreover, conventional methods of monitoring water stress do not take into account plants and soil heterogeneity, and their real evapotranspiration rates in the field have not been automated yet [20]. As a result, there is a growing interest in finding new affordable ways to estimate the specific plant status over space and time [17,64], e.g., by using multispectral images [32,50], as well as geometrical data, such as surface and volume of the canopy [59].

Unmanned aerial vehicles (UAVs) equipped with spectral cameras are capable of providing geo-referenced spectral information at high spatial resolution and at a reasonable cost [50,63]. However, the outcomes obtainable from UAV multispectral sensors can be influenced by external factors such as ground brightness, atmospheric conditions, soil humidity, and the specific characteristics of the sensor, with an effect on the spectral response in the field [19,63]. Over the years, more than 100 vegetation indexes (VIs) have been calculated from commonly measured multispectral bands in order to minimize the environmental effects [4].

Moreover, to assess the canopy status, size parameters (e.g., height, volume) can be obtained by processing 3D point clouds [67]. Experimental comparisons report higher accuracy of the geometric measurements retrieved by means of ground mapping systems with respect to those obtained by UAVs [35]. In this context, mobile robotics, combined with remote sensing techniques, can provide an important aid for monitoring and mapping [52]. In comparison to UAVs, ground robots can hold a higher payload, provide a closer field of view, and point clouds with higher density [29]. Furthermore, ground mobile robots have greater usability, flexibility, can perform analysis and manipulation on the ground, and are less weather dependent than aerial platforms.

Several examples of mobile robots mounting onboard Light Detection and Ranging (LiDAR) sensors to extract three-dimensional maps of plants and crops are described in the literature [42], thanks to their long range detection, high update rate, and independence from illumination. To broaden their use in reconstructing 3D point clouds, 2D LiDAR sensors are commonly arranged in such a way that the laser plane is perpendicular to the robot path [6,57]. For instance, a custom robot equipped with a 2D LiDAR sensor, mounted on a mast of adjustable height, is applied to map a vineyard in [47]. Similarly, the scan of an olive orchard is obtained with a 2D LiDAR sensor mounted on an all-terrain vehicle in [14]. A better option for point cloud reconstruction is 3D LiDAR technology. These sensors have indeed a larger field of view compared to 2D LiDAR devices and directly provide a dense point cloud of the surroundings, although they may have lower resolution and accuracy than 2D LiDAR sensors [10,52]. However, the main drawback of LiDAR solutions in horticulture occurs when performing the survey in rainy conditions, as the laser beams could be reflected by raindrops, producing noisy and inaccurate point clouds [61].

Nowadays, the reconstruction of the 3D point cloud of a surrounding environment is commonly performed by means of Simultaneous Localization and Mapping (SLAM) methods, which make it possible to build a 3D point cloud using subsequent scans only. However, the models obtained through SLAM approaches are mainly used for navigation purposes. Alternatively to SLAM, a 3D reconstruction of the surrounding environment can be created using a structure-from-motion (SfM) approach, integrating a sequence of images taken from different way points [21], or a multi-camera system composed of many sensors externally calibrated [58]. Nevertheless, a reconstruction based on SfM can be affected by small plant movements during data collection, for example by wind moving the leaves.

Environments with repetitive features can be problematic for LiDAR-based SLAM algorithms. For this reason, state-of-the-art SLAM algorithms often rely on sensor fusion techniques to additionally account for data from direct georeferencing systems [51]. For instance, a SLAM approach fusing LiDAR and inertial measurement unit (IMU) data is tested in a vineyard in [59]. Furthermore, LiDAR and GNSS data are fused together by means of SLAM to improve the robustness of the localization in [11].

Subsequently to the creation of a 3D point cloud, geometrical features can be extracted from the point cloud, e.g., by splitting the map with regular grids and summing the volumes of the filled voxels [47]. Another option is to generate a mesh encapsulating the whole points with triangulation algorithms like the Convex Hull [10] and the Alpha Shape [59].

The literature reports examples of geometric maps (built by using mobile robots) with additional spectral data (acquired by means of a spectral camera), e.g., the Normalized Difference Vegetation Index (NDVI) and the Normalized Difference Red Edge (NDRE). In [12], a NDVI map of a horticultural field is generated by a mobile robot equipped with RGB, multispectral, and hyperspectral cameras directed toward the plants. Similarly, NDVI mosaics of red cabbage rows are built in [54]. The lateral layout of spectral sensing devices is suitable for assessing the vegetation state of plants organized in rows [15,45]. For instance, examples of mobile robots, equipped with 2D LiDAR and Optrx Crop sensors to get both a precise volume reconstruction and NDVI mapping can be found in [5,41].

3D multispectral point clouds can also be obtained through photogrammetry, as in [30,56,62]. Furthermore, thermal point cloud can be generated using RGB and thermal images [26,60], as well as by applying thermal images and LiDAR data fusion for crop monitoring [34].

Data from ground robots, with targeted survey capabilities, and aerial vehicles can also be combined taking advantage of acquisitions from different points of view and different spatial scales, e.g., in [10,27–29,37]. There are very few studies in the literature providing understanding on how good is combining these two platforms. For instance, a comparison between the 3D point cloud obtained using the

agricultural robot Thorvald and the 3D orthomosaics acquired by a UAV can be found in [48]. In [38] the approximate reconstruction of broad regions from a UAV are refined using the local information collected by a mobile robot. Furthermore, in [65] the authors combine UAV and ground based RGB image data, showing advantages and flexibility in intra-tree inspection by checking its sub-volumes and avoiding occlusions, especially when the canopy density changes from the top to the bottom.

As far as the water status is concerned, an example where 3D images are used to extract drought information can be found in [7]. Furthermore, the authors in [60] adopted thermal infrared images and a binocular stereovision system to extract 3D point cloud and analyze the water stress in potato plants. Moreover, an algorithm for automated phenotyping through plant 3D modeling for the early detection of water stress can be found in [43]. However, to the best of the authors' knowledge, no examples of analysis of the effects of water regime on grapevine canopy status can be found in the present literature using data acquired by means of a UAV and a mobile robot.

In this work, we propose a novel approach for evaluating the effects of different water regimes on water potential, vegetation indexes, and geometrical data of the grapevine canopy, by combining geometric measurements acquired by a mobile robot with spectral data from a UAV, as well as traditional measurements, such as the stem and pre-dawn water potential. The main scientific contribution of this work is the analysis of the effects of water regimes on grapevine status using data from a UAV and a mobile robot that are coupled together to extract spectral information only in correspondence to the plants, avoiding surfaces not belonging to the canopy.

2. Materials and methods

2.1. Vineyard site and experimental design

The experiments were conducted in 2022 in a vineyard of the University of Udine (North Eastern Italy, Lat. 46°01'53.0"N, Long. 13°13'29.0"E, 113 m above sea level). The vineyard, consisting of Pinot gris clone R6 plants grafted on SO4 rootstock, was planted in 2013 with a plant density of 4000 plants/ha (1.0 m between vines × 2.5 m between rows) and a sub-irrigation system (Fig. 1). Vines were pruned using a single guyot training system and were planted in a gravely loam soil characterized by a good organic matter content.

Three adjacent rows of the vineyard were used for the experiments for a total experimental area of approximately of 117×10 m^2 (Fig. 2). For each distinct row, 3 plots composed of 12 homogeneous plants were selected, as shown in Fig. 1. From budburst to flowering the vines of all treatments were fully irrigated. Subsequently, a specific water regime was imposed for each experimental row in order to keep the average values of pre-dawn water potential (Ψ_{pd}) within predetermined boundaries. The Ψ_{pd} is often used as soil water potential indicator, this allowed a comparison of three water treatments (from flowering to harvest):

- well watered (WW), $\Psi_{pd} = -0.2$ MPa;
- moderate stress (MS), $\Psi_{pd} = -0.35$ MPa;
- severe stress (SS), $\Psi_{pd} = -0.55$ MPa.

The extensive experiments presented in this work involved the use of three distinct tools: a Scholander chamber for water potential measurements, a UAV for the acquisition of multispectral images, and a mobile robot for the 3D reconstruction of the plants. The collected data were analyzed to retrieve water potential, vegetation indexes, and geometrical measurements, as it is shown in Fig. 3. Data from the mobile robot and the UAV are tightly coupled in order to extract spectral information from specific regions of interest and analyze the spatial variability of plants. The multispectral images obtained by the UAV are indeed segmented using the point clouds reconstructed by means of the mobile robot in order to compute the vegetation indexes only in correspondence to the real area of the plants, avoiding non-canopy surfaces. Furthermore, differently from other works [30,56], a mobile robot is used for 3D canopy reconstruction to avoid possible occlusions and erroneous volume estimations due to the canopy density changes from the top to the bottom.

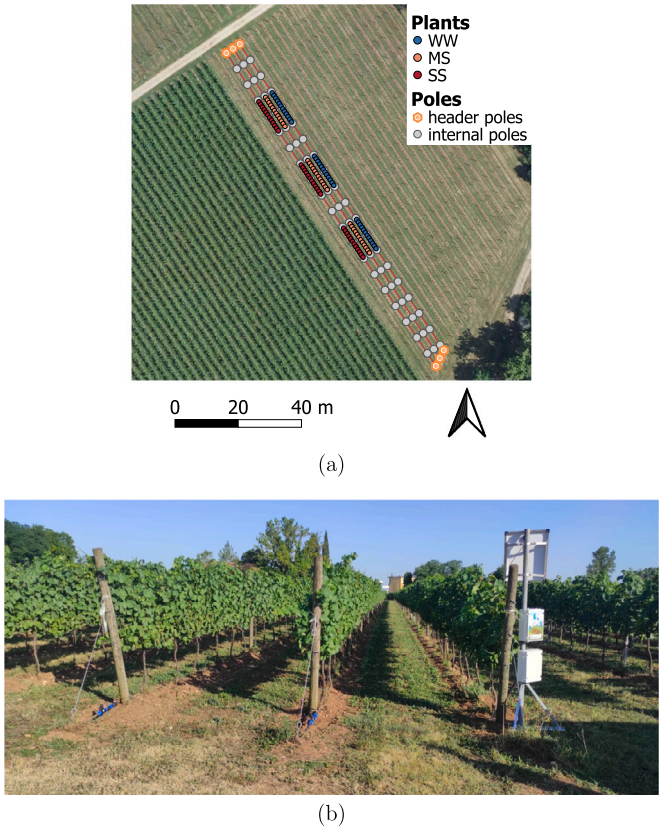

Fig. 1. Vineyard site: (a) the location of plants, header, and internal poles in a top view of the vineyard (true ortofoto RAFVG 2017-2020, provided by IRDAT under IODL 2.0 license, was used as background layer); (b) entrance of the vineyard rows showing the irrigation control unit and part of the sub-irrigation system.

2.2. Physiological measurements

The water status of the plants was monitored by measuring the stem water potential (Ψ_{stem}) and the pre-dawn water potential (Ψ_{pd}). All water potential measurements were carried out on 28/07/2022, 62 days after full bloom (DAFB), using a Scholander chamber (Soil Moisture Corp., USA), following the indications described by [46]. The measurements of Ψ_{stem} and Ψ_{pd} were respectively performed on nine samples for each water regime ($n = 27$), i.e., three individual leaves collected from different plants belonging to each of the three plots.

2.3. Acquisition of multispectral indexes using a UAV

The acquisition campaign of the aerial data was conducted on a single flight at midday on 28/07/2022 (62 DAFB) under optimal weather conditions, using a DJI P4 multispectral UAV (SZ DJI Technology Co., Ltd., Beijing, China) equipped with a RTK-GNSS module of the same manufacturer (Fig. 4). This compact UAV is provided with six cameras, one of which captures RGB images and the other five distinct spectral bands: blue (450 nm ± 16 nm), green (560 nm ± 16 nm), red (650 nm ± 16 nm), red-edge (730 nm ± 16 nm), near-infrared (840 nm ± 26 nm). The flight was conducted at an above-ground level of 20 m, covering an

(a) (b) (c)

Fig. 2. Inspected vineyard rows: (a) well watered row; (b) medium stressed row; (c) severe stressed row.

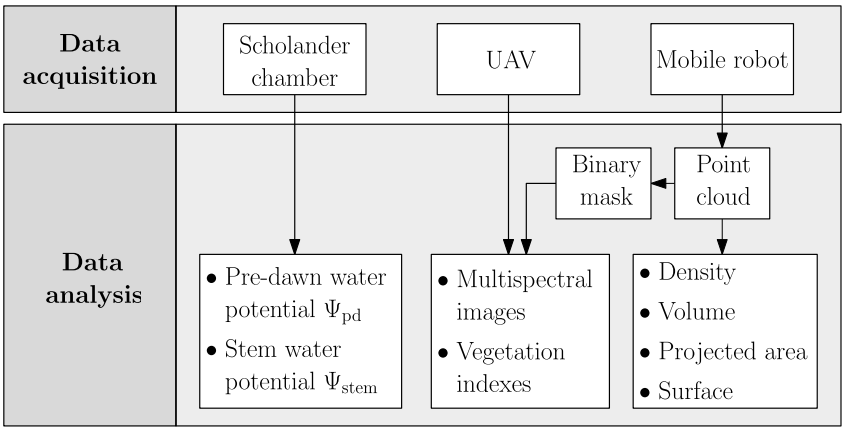

Fig. 3. Description of the data acquisition and analysis.

(a) (b)

Fig. 4. (a) The DJI P4 multispectral UAV; (b) the multispectral and RGB cameras.

area of about 0.48 ha. 2220 pictures were sampled with the UAV during the flight and processed using the PIX4Dmapper software (version 4.8.0; PiX4D, Switzerland), obtaining multispectral and RGB georeferenced rasters. The subsequent data management and processing were performed in the EPSG 6708 reference system (RDN2008 / UTM zone 33N (N-E)).

To relate the physiological measurements with the multispectral data, the five spectral bands were used to calculate the sixty vegetation indexes (feasible with the bands of the light spectrum acquired by the UAV camera) described in [18]. An overabundant set of VIs, compared to the few spectral indexes commonly used to monitor stress factors, were considered. All VIs have been calculated as raster operations using the packages *terra* and *raster* of the R Statistical language (version 4.2.2; R CoreTeam, Austria).

A correlation analysis is performed between the mean plot values of the stem water potential and the vegetation indexes. The highest squared value R^2, and the lowest p-value are used to select nine representative indexes among the sixty computed. The nine aforementioned VIs can be related to four of the five categories of potential use of indexes reported in [18]. These categories differ in the combinations of spectral bands used. Table 1 reports the selected VIs, the bands, the equations used for their computation, and the usage category. The category related to biomass and vegetation density, mainly characterized by the combination of NIR and red bands, is prevalent.

2.4. Acquisition of the canopy status using a mobile robot

The mobile robotic platform Scout 2.0 (AgileX Robotics, Shenzen, China) shown in Fig. 5 was used to collect the point clouds of the vineyard on 26/07/2022 (60 DAFB). The mobile robot is provided with four electric motors and equipped with a Jetson Xavier (NVIDIA, Santa Clara, USA) onboard computer (Octal-core NVIDIA Carmel ARMv8.2 CPU @ 2.26GHz; 512-core Volta GPU @ with 64 Tensor Cores; 32GB 256-bit LPDDR4x @ 2133MHz), a RealSense D435 (Intel, Santa Clara, USA) camera, and a VLP-16 (Velodyne, Santa Clara, USA) LiDAR sensor featuring 16 channels. The VLP-16 has a range up to 100 m, an accuracy of ±3 cm, a 360° horizontal field of view, and a 30° vertical field of view (±15°). The coordinate system of the LiDAR sensor is shown in Fig. 5b.

During the data acquisition campaign, the robot was teleoperated moving along four corridors of the vineyard, long approximately 117 m, returning to the starting point. In this way, the plants of the three considered vineyard rows were scanned from each side.

The data from the LiDAR sensor was acquired in ROS Melodic using Ubuntu 18.04 in the ROS Bags file format. To reconstruct the 3D environment using SLAM, the ROS Bags files were reproduced at the rate they were recorded on a workstation (Intel Core i5-10600K CPU @ 4.1GHz × 12; 32 GB RAM; 64-bit OS) running Ubuntu 18.04 and ROS Melodic. The 3D reconstruction of the vineyard was obtained with the graph-based SLAM algorithm Real-Time Appearance-Based Mapping (RTAB-Map) [22], which performs the scan matching by using the

Table 1
Description of the nine selected VIs: equations and usage category [18].

Water potential	VI	Equation	Usage category
Ψ_{pd}/Ψ_{stem}	GDVI	NIR − G	Biophysical parameters
Ψ_{pd}/Ψ_{stem}	PVI	$\sqrt{(0.335NIR - 0.149R)^2 + (0.335R - 0.149NIR)^2}$	Biomass/vegetation density
Ψ_{pd}/Ψ_{stem}	TGI	G − 0.39R − 0.61B	Pigments
Ψ_{stem}	2GRBi	2G − (R + B)	Pigments
Ψ_{stem}	DVI	NIR − R	Biomass/vegetation density
Ψ_{stem}	EVI2	2.5(NIR − R)/(NIR + 2.4R + 1)	Biomass/vegetation density
Ψ_{stem}	MCARI1	1.2(2.5(NIR − R) − 1.3(NIR − G))	Chlorophyll
Ψ_{stem}	MRVI	(R − 1)/(NIR − 1)	Biomass/vegetation density
Ψ_{stem}	MTVI1	1.2(1.2(NIR − G) − 2.5(R − G))	Biophysical parameters

Fig. 5. (a) The Scout 2.0 mobile robot; (b) close view of the robot electronics and LiDAR sensor.

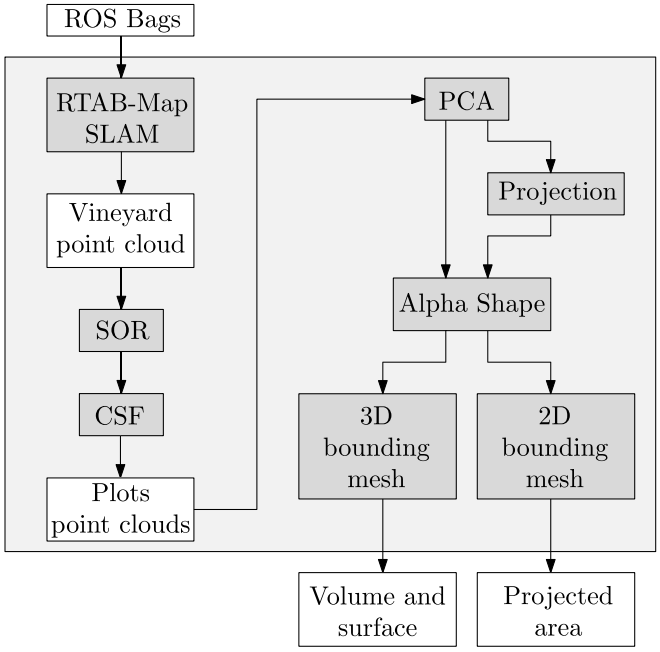

Fig. 6. Overview on the point cloud processing.

Iterative Closest Point (ICP) algorithm with a point-to-plane registration and a loop closure optimization.

The 3D point cloud obtained with the SLAM algorithm was then processed with the open-source CloudCompare software, and each considered row was extracted from the whole point cloud. An overview on the point cloud processing is shown in Fig. 6. The Statistical Outlier Removal (SOR) filter [44] was applied to remove outliers and noise points caused by the motion of the LiDAR sensor during each scan. 20 neighboring points and a standard deviation multiplier equal to 1.00 were selected for the SOR filter. Moreover, the Cloth Simulation Filter (CSF) [66] was applied to separate ground points from those belonging to plants, using a cloth resolution (the grid size of cloth used to cover the terrain) of 0.5 m, a maximum number of iterations of 1000, and a classification threshold equal to 0.5. The SOR filter was applied before the CSF since the point cloud provided by RTAB-Map is noisy, mostly on the ground, and reducing the noise improves the outcome of the CSF.

Two binary masks (images with 0 in regions without vegetation and 1 in regions with plants) were applied in the QGIS software (version 3.22.11-Białowieża; QGIS.ORG, Switzerland) by projecting the filtered point cloud on the ground, i.e., along the vertical axis. Considering the image I, the set of pixels $\{p(i,j)\}$ of the vineyard plots can be represented as a subset $V \subset I$, where $(i,j) \in V$ if and only if the pixel $p(i,j)$ belongs to the plots. The binary mask is thus obtained with the following:

$$p(i,j) = \begin{cases} 1, & \text{if } (i,j) \in V \\ 0, & \text{otherwise} \end{cases} \quad (1)$$

The first binary mask was obtained with points at the height of plant trunks, whereas the second one by using the whole point cloud. The first binary mask was used for georeferencing the second one in the EPSG 6708 reference system exploiting the *raster georeferencer tool* available in the QGIS software. The header poles (shown in Fig. 1) clearly visible in the trunks mask were used as landmarks. Subsequently, a segmentation of the vineyard plots was performed through the second binary mask.

Three plots for each row were extracted from the sections of the point cloud by measuring the distances from the vineyard header pole. The point density was computed in CloudCompare for each point by considering the neighboring points over a radius of 0.1 m. To retrieve the estimates of the volume and surface of the plants, the Alpha Shape algorithm [13] implemented in Matlab® (version R2022b; The MathWorks Inc.®, Natick, MA, USA) was used. For each point cloud, the critical radius α^*, i.e., the smallest radius that builds a bounding area or volume through the triangulation (mesh) enclosing all points, was automatically selected in Matlab® to create the bounding mesh. The mesh triangles adjacent to the vineyard plot section planes were not considered in the computation of the surface since they do not represent the actual geometry of the plot.

To further investigate the canopy size in the considered rows of the vineyard, the area of the plants projected on the ground plane was computed. For this purpose, the axis along which to project the point cloud was retrieved by means of the Principal Component Analysis (PCA) technique. After the definition of the three principal directions, a 2D set of points was obtained by projecting the points along the vertical axis. The projected area was then calculated by applying the Alpha Shape algorithm to each of the 2D set of points. A description of the algorithm implemented in Matlab® to retrieve the size measurements is shown in Algorithm 1.

2.5. Statistical analysis

A statistical analysis has been provided for the evaluation of the outcomes. The eventual correlation between numerical variables, i.e., physiological measurements, multispectral indexes, and geometrical values, was studied by means of the one-way ANOVA test. When the test was significant, the averages are separated using the posthoc Tukey test (p-value < 0.05). The Shapiro-Wilk and Levene's tests were performed

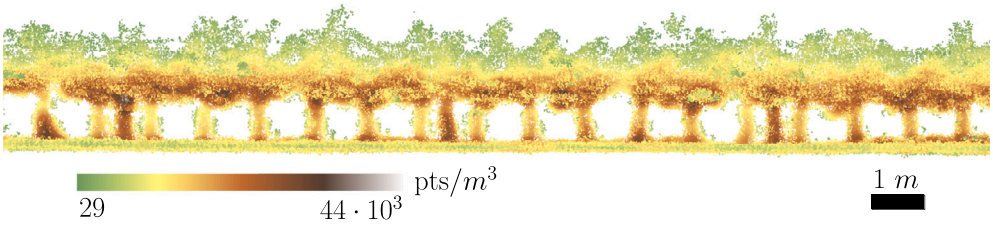

Fig. 7. 3D reconstruction of an example portion of a vineyard row (side view). The colors represent different values of points density.

Algorithm 1 Analysis of the point cloud.

Input: Point cloud data
Output: Bounding mesh *volume*, *surface*, and *projected area*
Import point cloud
Perform PCA analysis to define the principal axis
Compute α^* for the 3D bounding mesh
Compute the 3D bounding mesh using the Alpha Shape algorithm
Compute *volume* and *surface* of the 3D bounding mesh
Project the point cloud along the vertical axis
Compute α^* for the 2D bounding mesh
Compute the 2D bounding mesh using the Alpha Shape algorithm
Compute the *projected area* of the 2D bounding mesh

Table 2
Results of the one-way ANOVA analysis performed on physiological and geometrical parameters. In case of significant results of the ANOVA test, mean values are separated using the posthoc Tukey test. n.s.: not significative; ∗: p-value < 0.05; ∗∗: p-value < 0.01.

Parameter	Unit	Water regime			Result
		WW	MS	SS	
Ψ_{stem}	MPa	-0.57 ± 0.10	-0.75 ± 0.10	-0.98 ± 0.09	∗∗
Ψ_{pd}	MPa	-0.12 ± 0.01	-0.16 ± 0.01	-0.18 ± 0.02	∗∗
Canopy volume	m^3	6.37 ± 0.92	5.60 ± 0.18	4.80 ± 0.89	n.s.
Surface	m^2	50.07 ± 0.30	48.85 ± 6.84	50.95 ± 3.26	n.s.
Projected area	m^2	8.70 ± 0.33	7.83 ± 0.52	6.99 ± 0.42	∗
Points density	pts/m^3	20616 ± 1352	20674 ± 536	21539 ± 889	n.s.

to check for the normality of residuals and homogeneity of variance, respectively. Moreover, Spearman linear correlations are tested between the studied variables.

3. Experimental results

Fig. 7 illustrates a 3D reconstruction of an example portion of a vineyard row, where colors represent different values of point density. As it can be seen from the figure, points density changes from the top to the bottom of the canopy. An example of the reconstruction of the 3D bounding mesh of a vineyard experimental plot, and of the 2D bounding mesh of the projected area, starting from the 3D point cloud acquired by the mobile robot, is reported in Fig. 8. In the figure, the black dashed axis represent the principal axis of the 3D point cloud. Furthermore, the outcomes of the segmentation are shown in Fig. 9, where a top view of the plot masks used in the experiments is reported using the NIR band as background, together with a magnifications of the plots.

The outcomes of the one-way ANOVA analysis performed on physiological and geometrical parameters are shown in Table 2, in which mean values and standard deviations are reported together with the result of the post-hoc Tukey test. The last column of Table 2 indicates the significance of the results. The normality of residuals and homogeneity of variances are confirmed by the statistical tests (data not reported).

The results of the measurements carried out with the Scholander chamber are first evaluated. Statistical differences are assessed by means of box plots (Fig. 10), which refer to a specific water regime (WW, MS, and SS) applied to a specific vineyard row. As expected, the WW and SS treatments are statistically different, with MS confirmed as an intermediate regime (Ψ_{stem}: p-value = 0.00775, Ψ_{pd}: p-value = 0.00697), both for Ψ_{stem} (Fig. 10a) and Ψ_{pd} (Fig. 10b). A positive trend is found between the water potential values and the applied water regimes: as the water supply increases, the water potential values improve. Considering the similar trends between Ψ_{pd} and Ψ_{stem}, it is possible to discern a distinct difference between the three water regimes applied to the three tested rows.

Fig. 11 shows the results of the correlation analysis between the stem water potential and the nine selected VIs. The obtained regression lines together with grey areas indicating the confidence interval (95%) are reported. The p-values of the VIs indicate significant differences between the group of analyzed samples. The nine VIs show strong positive correlations with stem water potential (GDVI: $R^2 = 0.90$, PVI: $R^2 = 0.90$, TGI: $R^2 = 0.87$, 2GRBi: $R^2 = 0.84$, DVI: $^2 = 0.78$, EVI2: $R^2 = 0.78$, MCARI1: $R^2 = 0.78$, MRVI: $R^2 = 0.78$, MTVI1: $R^2 = 0.78$).

Correlations between pre-dawn water potentials and VIs are established by means of the same procedure used for the stem water potential. The obtained regression lines together with grey areas indicating the confidence interval (95%) are depicted for Ψ_{pd} in Fig. 12. Only three VIs with a R^2 greater than 0.5 are reported: the TGI: $R^2 = 0.77$; the GDVI: $R^2 = 0.57$; the PVI: $R^2 = 0.57$. The VIs exhibit positive correlations with the pre-dawn water potential. These VIs, as well as the Ψ_{pd}, are mostly related to soil water content, thus they confirm the three different water regimes applied in the field.

The box plots in Fig. 13 report the geometrical measurements with respect to the water regime applied. The estimated canopy volume, surface, and projected area, depicted in Fig. 13a, Fig. 13b, and Fig. 13c respectively, show a positive trend with the water regime applied. Furthermore, the values of projected area relative to the WW water regime are statistically different with respect to the SS, as reported Table 2. No statistical differences are found between the three considered water regimes with respect to the volume of the canopy, density of the point clouds, and the surface. However, there is a trend between the average volume values belonging to each water treatment. Specifically, compared to the average values of the MS, there is an increase in the volume of 13.75% for the WW regime and a reduction of 14.29% for the SS regime, whereas the WW is increased by the 32.71% with respect to the SS.

A regression analysis is performed to correlate the geometrical measurement with those of the Scholander chamber. A highly effective correlation is obtained between the stem water potential and the canopy volume as well as between the stem water potential and the projected area. Fig. 14 reports the results of the regression with lines, whereas the grey areas indicate the confidence interval (95%). Positive correlations are obtained between these two geometrical measurements and the stem water potential values. Both regressions present significant p-values, whereas the obtained R^2 values are 0.72 and 0.67 for the canopy volume and the projected area, respectively.

4. Discussion

The combined utilization of UAV and a mobile robot proved advantageous in acquiring the spatial variability of grapevine canopy identified through the masks. The masks facilitated the extraction of spectral data from the UAV exclusively pertaining to the canopy, thereby mitigating potential interference from extraneous factors such as soil and

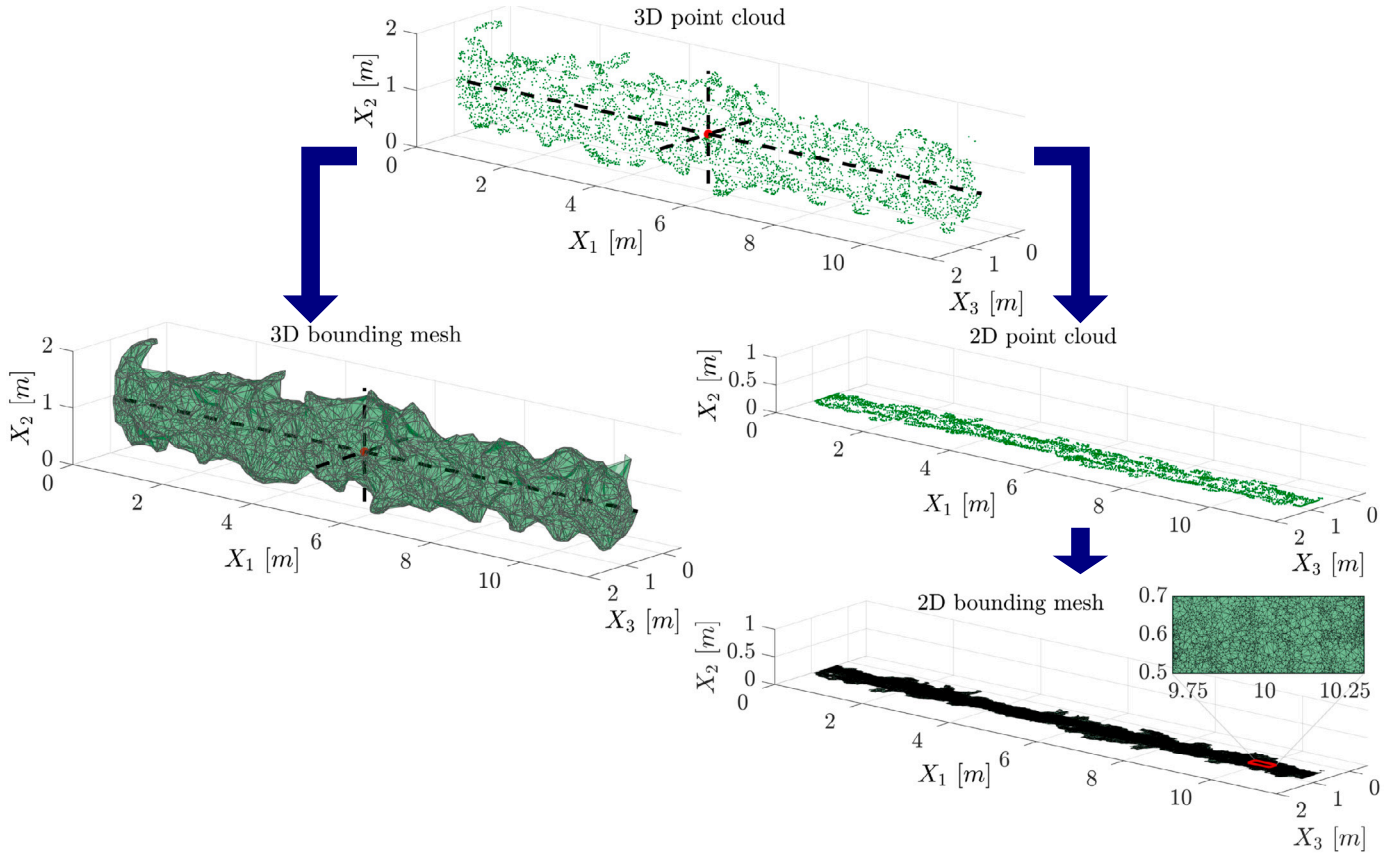

Fig. 8. Example of the reconstruction of the 3D bounding mesh of a vineyard experimental plot (left), and of the 2D bounding mesh of the projected area (right), starting from the 3D point cloud acquired by the mobile robot. Black dashed axis represent the principal axis of the 3D point cloud.

inter-row weeds. The robustness of the relationship between the extracted indexes and the physiological measurements is also evidenced by the high values of R^2 observed in the correlations. Furthermore, the results of this study indicate that incorporating a broader range of vegetation indexes can enhance our understanding of the actual condition of plants. The results are positive for both measures of plant water potential, providing insights for future uses of VIs both for the assessment of plant water stress (stem water potential) and to obtain indications on soil water content (pre-dawn water potential).

The values of canopy volume and projected area acquired by means of the mobile robot further confirm the effect of the three different water regimes on the growth of the plants. To this regards, it should be emphasized that the use of a ground robot in combination with a UAV for 3D grapevine canopy reconstruction shows advantages and flexibility in intra-tree inspection by checking sub-volumes and avoiding occlusions, especially when canopy density changes from the top to the bottom.

The outcomes in terms of volume and projected area are consistent with our expectations from an agronomic standpoint: the reduced aerial growth of water-stressed plants [1,53] results in different volume and projected area with higher values in well-watered plants. It is important to note that the differences found are not directly related to the water content. Among the VIs designed for inspecting the water status of the vineyard, those belonging to the water content category are characterized by the combination of NIR and SWIR bands [18]. The DJI P4 UAV and other drones currently used for agricultural research are not equipped to acquire the SWIR band, thus the computation of that kind of indexes is not possible. However, the resulting indexes obtained in this work are more geometric-related (as reported in the last column of Table 1), with a high correlation to indexes often used for the assessment of biomass and vegetation density.

In this experiment, the water status of plants was controlled since bloom, and plants had the time to differentiate their growth. The difference in canopy volume and surface depends on the amount of water applied, as we can appreciate in Fig. 13. Different results may be achieved in the case of an apriori non-controlled water regime or in the case of the application of temporary water stress, in which geometrical measurements could not be used as a proxy of the plant water status. Moreover, in the aforementioned situations, associating VIs related to biomass and vegetation density with VIs related to plant physiological activity can be useful in the analysis of the plant canopy status. In that case, VIs used for chlorophyll, pigments, and biophysical parameters can be included (Table 1). Finally, from the results of the experiment, it is possible to observe that the VIs that performed best in our survey are different from those usually employed by the classical studies that use mobile robots, such as the NDVI or the NDRE [5,35].

The proposed approach is suitable for studying the effect of a controlled water regime that impacts plant development and thus canopy size (Fig. 13 and 14). However, our approach could not be eligible to detect temporary water stress. In that case, alternative approaches should be adopted, as for instance thermal remote sensing [23].

In future field applications, the proposed approach will be used to acquire measurements across a season, as in [36], in order to extrapolate the relationships between water regime, vegetation indexes, and geometrical data over an extended period of time. Furthermore, we will extend the approach to analyze plants under temporary water stress, by mounting a multispectral camera on the mobile robot. In future developments, both the navigation of the robot and data processing will be fully automated, thereby minimizing the requirement for human intervention. Finally, deep learning approaches [9,39] will also be considered to detect vineyard plants stress in situ from images captured by drones and ground robots.

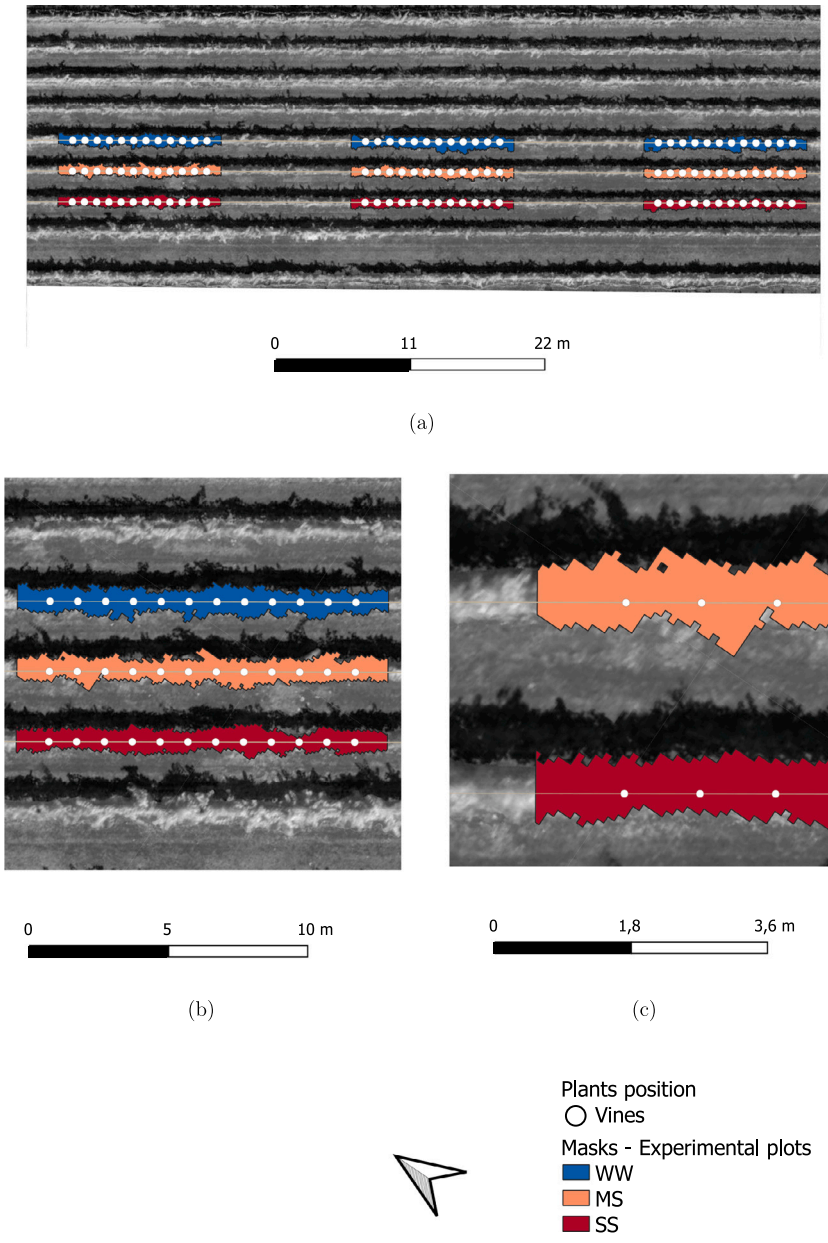

Fig. 9. (a) Top view of the plot masks used in the experiments (the NIR band is used as background); (b) and (c) magnifications of the plots.

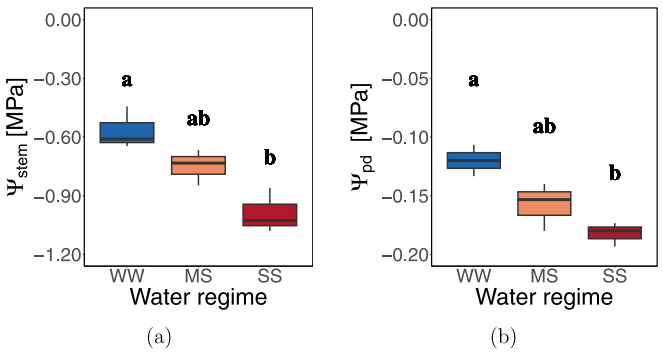

Fig. 10. Results of water potential measured with the Scholander chamber: (a) stem water potential; (b) pre-dawn water potential. In case of significant results of the one-way ANOVA test, mean values are separated using the post-hoc Tukey test. Different letters indicate statistically significant difference. Variables with no common letters are significantly different.

5. Conclusion

In this paper, a novel approach for analyzing the effects of water regime on grapevine canopy status using robotics as an aid for monitoring and mapping has been proposed. Data from an unmanned aerial vehicle (UAV) and a ground mobile robot have been used to obtain multispectral images and multiple vegetation indexes, and the 3D reconstruction of the canopy, respectively. Unlike previous works, sixty vegetation indexes have been computed precisely by using the projected area of the vineyard point cloud as a mask. Extensive experimental tests on repeated plots of Pinot gris vines have shown that the GDVI, PVI, and TGI vegetation indexes are positively correlated with the water potential: GDVI ($R^2 = 0.90$ and 0.57 for the stem and pre-dawn water potential, respectively), PVI ($R^2 = 0.90$ and 0.57), TGI ($R^2 = 0.87$ and 0.77). Furthermore, the canopy volume and the canopy area projected on the ground are impacted by the water status, as well as stem and pre-dawn water potential measurements. The results obtained in this work demonstrated the feasibility of the proposed approach and the potential of robotic technologies, supporting precision viticulture.

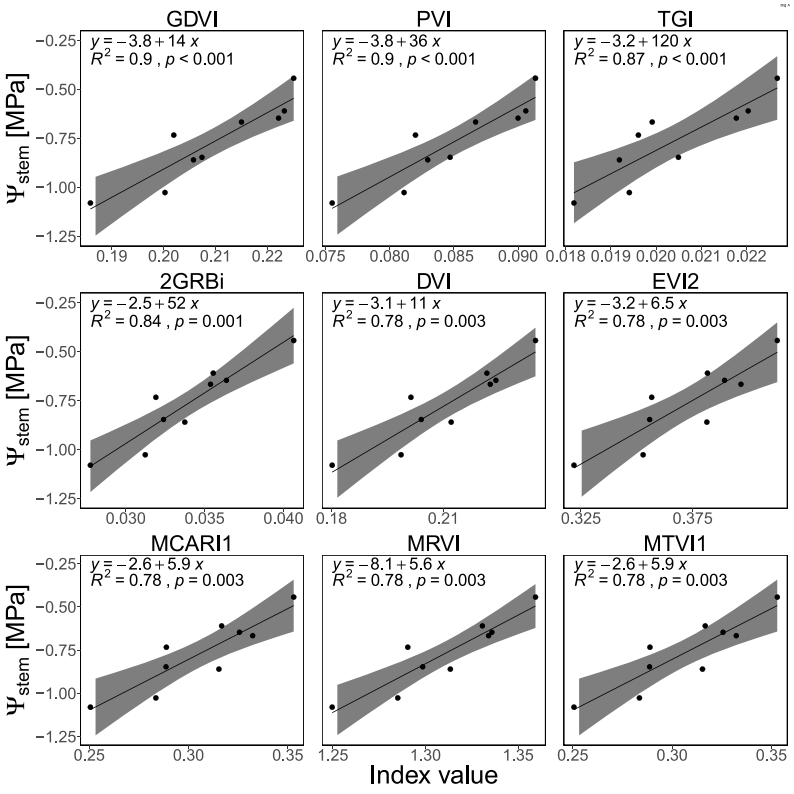

Fig. 11. Results of the correlation analysis between the stem water potential and the vegetation indexes. Points indicate the mean values of the plot stem water potential correlated with the mean values of the VIs of the plot. The black line represents the regression line, and the grey area indicates the confidence interval (95%). The regression line equation, R^2, and the Spearman correlation coefficient are reported for each plot on the top-left side.

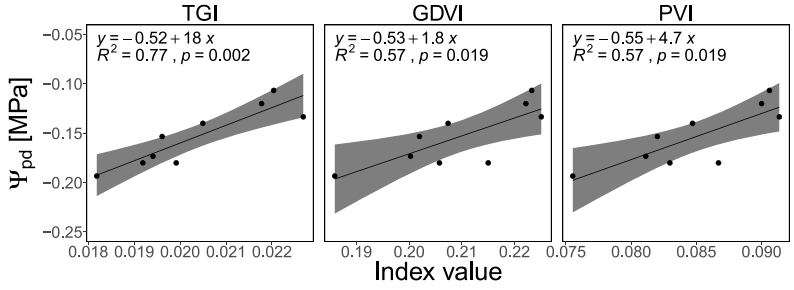

Fig. 12. Results of the correlation analysis between the pre-dawn water potential and the vegetation indexes. Points indicate the mean values of the plot pre-dawn water potential correlated with the mean values of the VIs of the plot. The black line represents the regression line, and the grey area indicates the confidence interval (95%). The regression line equation, R^2, and the Spearman correlation coefficient are reported for each plot on the top-left side.

Declaration of competing interest

The authors declare that they have no known competing financial interests or personal relationships that could have appeared to influence the work reported in this paper.

Data availability

Data will be made available on request.

Acknowledgements

The authors would like to thank Dr. Eleonora Maset for her suggestions on the processing of the point clouds, and Mr. Michele Mestroni for having provided the UAV used in this work.

Funding

This study was carried out within the Agritech National Research Center and received funding from the European Union Next-Generation EU (Piano Nazionale di Ripresa e Resilienza (PNRR) – Missione 4 Componente 2, Investimento 1.4 - D.D. 1032 17/06/2022, CN00000022). This manuscript reflects only the authors' views and opinions, neither the European Union nor the European Commission can be considered responsible for them.

This research was partially developed within the Laboratory for Big Data, IoT, Cyber Security (LABIC) funded by Friuli Venezia Giulia Region, and the Laboratory for Artificial Intelligence for Human-Robot Collaboration (AI4HRC) funded by Fondazione Friuli.

The first author acknowledges support from the National Ph.D. Programme in Artificial Intelligence of University of Naples Federico II (Naples, Italy).

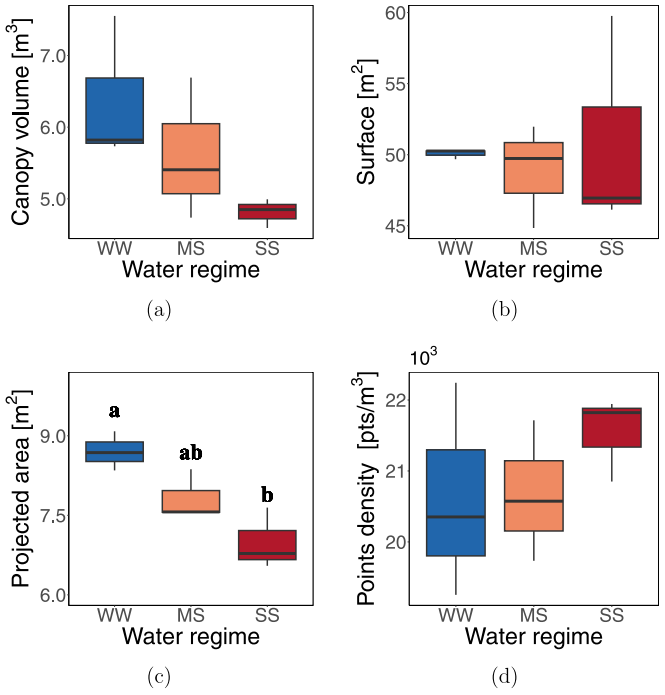

Fig. 13. Results of the 3D reconstruction of the canopy: (a) volume; (b) bounding surface; (c) projected area; (d) points density. In case of significant results of the one-way ANOVA test, mean values are separated using the post-hoc Tukey test. Different letters indicate statistically significant difference. Variables with no common letters are significantly different.

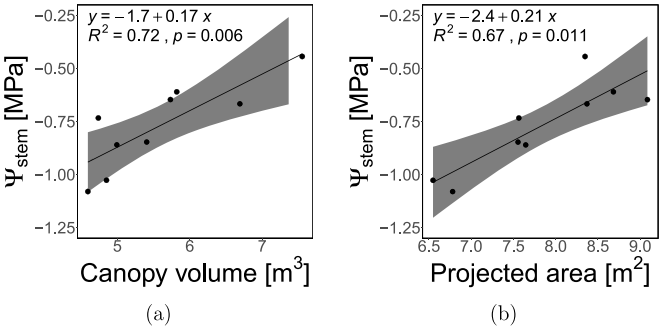

Fig. 14. Results of the correlation analysis between the stem water potential and the geometrical measurements: (a) canopy volume; (b) projected area. Points indicate the mean values of the plot stem water potential correlated with the mean values of canopy volume and projected area of the plot. The black line represents the regression line, and the grey area indicates the confidence interval (95%). The regression line equation, R^2, and the Spearman correlation coefficient are reported for each plot on the top-left side.

References

[1] S. Álvarez, M.J. Sánchez-Blanco, Changes in growth rate, root morphology and water use efficiency of potted Callistemon citrinus plants in response to different levels of water deficit, Sci. Hortic. 156 (2013) 54–62.

[2] P. Arias, N. Bellouin, E. Coppola, R. Jones, G. Krinner, J. Marotzke, V. Naik, M. Palmer, G.K. Plattner, J. Rogelj, et al., Climate Change 2021: The Physical Science Basis. Contribution of Working Group I to the Sixth Assessment Report of the Intergovernmental Panel on Climate Change, Technical Summary, IPCC Intergovernmental Panel on Climate Change, 2021.

[3] H. Bandurska, Drought stress responses: coping strategy and resistance, Plants 11 (2022) 922.

[4] A. Bannari, D. Morin, F. Bonn, A. Huete, A review of vegetation indices, Remote Sens. Rev. 13 (1995) 95–120.

[5] M. Bietresato, G. Carabin, D. D'Auria, R. Gallo, G. Ristorto, F. Mazzetto, R. Vidoni, A. Gasparetto, L. Scalera, A tracked mobile robotic lab for monitoring the plants volume and health, in: 2016 12th IEEE/ASME International Conference on Mechatronic and Embedded Systems and Applications (MESA), IEEE, 2016, pp. 1–6.

[6] M. Bietresato, G. Carabin, R. Vidoni, A. Gasparetto, F. Mazzetto, Evaluation of a LiDAR-based 3D-stereoscopic vision system for crop-monitoring applications, Comput. Electron. Agric. 124 (2016) 1–13.

[7] N. Briglia, K. Williams, D. Wu, Y. Li, S. Tao, F. Corke, G. Montanaro, A. Petrozza, D. Amato, F. Cellini, et al., Image-based assessment of drought response in grapevines, Front. Plant Sci. 11 (2020) 595.

[8] T. Brodribb, C.R. Brodersen, M. Carriqui, V. Tonet, C. Rodriguez Dominguez, S. McAdam, Linking xylem network failure with leaf tissue death, New Phytol. 232 (2021) 68–79.

[9] M. Cándido-Mireles, R. Hernández-Gama, J. Salas, Detecting vineyard plants stress in situ using deep learning, Comput. Electron. Agric. 210 (2023) 107837.

[10] M. Chakraborty, L.R. Khot, S. Sankaran, P.W. Jacoby, Evaluation of mobile 3D Light Detection and Ranging based canopy mapping system for tree fruit crops, Comput. Electron. Agric. 158 (2019) 284–293.

[11] F.A.A. Cheein, J. Guivant, SLAM-based incremental Convex Hull processing approach for treetop volume estimation, Comput. Electron. Agric. 102 (2014) 19–30.

[12] S. Cubero, E. Marco-Noales, N. Aleixos, S. Barbé, J. Blasco, Robhortic: a field robot to detect pests and diseases in horticultural crops by proximal sensing, Agriculture 10 (2020) 276.

[13] H. Edelsbrunner, D. Kirkpatrick, R. Seidel, On the shape of a set of points in the plane, IEEE Trans. Inf. Theory 29 (1983) 551–559.

[14] A. Escolà, J.A. Martínez-Casasnovas, J. Rufat, J. Arnó, A. Arbonés, F. Sebé, M. Pascual, E. Gregorio, J.R. Rosell-Polo, Mobile terrestrial laser scanner applications in precision fruticulture/horticulture and tools to extract information from canopy point clouds, Precis. Agric. 18 (2017) 111–132.

[15] J. Fernández-Novales, V. Saiz-Rubio, I. Barrio, F. Rovira-Más, A. Cuenca-Cuenca, F. Santos Alves, J. Valente, J. Tardaguila, M.P. Diago, Monitoring and mapping vineyard water status using non-invasive technologies by a ground robot, Remote Sens. 13 (2021) 2830.

[16] E. Garnier, A. Berger, Testing water potential in peach trees as an indicator of water stress, J. Hortic. Sci. 60 (1985) 47–56.

[17] D. Gautam, V. Pagay, A review of current and potential applications of remote sensing to study the water status of horticultural crops, Agronomy 10 (2020) 140.

[18] R. Giovos, D. Tassopoulos, D. Kalivas, N. Lougkos, A. Priovolou, Remote sensing vegetation indices in viticulture: a critical review, Agriculture 11 (2021) 457.

[19] S. Huang, L. Tang, J.P. Hupy, Y. Wang, G. Shao, A commentary review on the use of normalized difference vegetation index (NDVI) in the era of popular remote sensing, J. Forest. Res. 32 (2021) 1–6.

[20] S.O. Ihuoma, C.A. Madramootoo, Recent advances in crop water stress detection, Comput. Electron. Agric. 141 (2017) 267–275.

[21] S. Jay, G. Rabatel, X. Hadoux, D. Moura, N. Gorretta, In-field crop row phenotyping from 3D modeling performed using Structure from Motion, Comput. Electron. Agric. 110 (2015) 70–77.

[22] M. Labbé, F. Michaud, RTAB-Map as an open-source LiDAR and visual simultaneous localization and mapping library for large-scale and long-term online operation, J. Field Robot. 36 (2019) 416–446.

[23] L.N. Lacerda, J.L. Snider, Y. Cohen, V. Liakos, S. Gobbo, G. Vellidis, Using UAV-based thermal imagery to detect crop water status variability in cotton, Smart Agricult. Technol. 2 (2022) 100029.

[24] Y. Lei, H. Zhang, F. Chen, L. Zhang, How rural land use management facilitates drought risk adaptation in a changing climate—a case study in arid northern China, Sci. Total Environ. 550 (2016) 192–199.

[25] C. Lesk, P. Rowhani, N. Ramankutty, Influence of extreme weather disasters on global crop production, Nature 529 (2016) 84–87.

[26] A. López, J.M. Jurado, C.J. Ogayar, F.R. Feito, An optimized approach for generating dense thermal point clouds from UAV-imagery, ISPRS J. Photogramm. Remote Sens. 182 (2021) 78–95.

[27] M. Mammarella, L. Comba, A. Biglia, F. Dabbene, P. Gay, Cooperation of unmanned systems for agricultural applications: a case study in a vineyard, Biosyst. Eng. 223 (2022) 81–102.

[28] M. Mammarella, L. Comba, A. Biglia, F. Dabbene, P. Gay, Cooperation of unmanned systems for agricultural applications: a theoretical framework, Biosyst. Eng. 223 (2022) 61–80.

[29] R. Manish, Y.C. Lin, R. Ravi, S.M. Hasheminasab, T. Zhou, A. Habib, Development of a miniaturized mobile mapping system for in-row, under-canopy phenotyping, Remote Sens. 13 (2021) 276.

[30] R. Martínez-Peña, S. Vélez, R. Vacas, H. Martín, S. Álvarez, Remote sensing for sustainable pistachio cultivation and improved quality traits evaluation through thermal and non-thermal UAV vegetation indices, Appl. Sci. 13 (2023) 7716.

[31] J. Martinez-Vilalta, R. Poyatos, D. Aguade, J. Retana, M. Mencuccini, A new look at water transport regulation in plants, New Phytol. 204 (2014) 105–115.

[32] A. Matese, S.F. Di Gennaro, Beyond the traditional NDVI index as a key factor to mainstream the use of UAV in precision viticulture, Sci. Rep. 11 (2021) 1–13.

[33] N.G. McDowell, Mechanisms linking drought, hydraulics, carbon metabolism, and vegetation mortality, Plant Physiol. 155 (2011) 1051–1059.

[34] F.J.Y. Narváez, J.S. del Pedregal, P.A. Prieto, M. Torres-Torriti, F.A.A. Cheein, LiDAR and thermal images fusion for ground-based 3D characterisation of fruit trees, Biosyst. Eng. 151 (2016) 479–494.

[35] A. Pagliai, M. Ammoniaci, D. Sarri, R. Lisci, R. Perria, M. Vieri, M.E.M. D'Arcangelo, P. Storchi, S.P. Kartsiotis, Comparison of aerial and ground 3D point clouds for canopy size assessment in precision viticulture, Remote Sens. 14 (2022) 1145.
[36] R. Polvara, S. Molina, I. Hroob, A. Papadimitriou, K. Tsiolis, D. Giakoumis, S. Likothanassis, D. Tzovaras, G. Cielniak, M. Hanheide, Bacchus Long-Term (BLT) data set: acquisition of the agricultural multimodal BLT data set with automated robot deployment, J. Field Robot. (2023).
[37] C. Potena, R. Khanna, J. Nieto, R. Siegwart, D. Nardi, A. Pretto, AgriColMap: aerial-ground collaborative 3D mapping for precision farming, IEEE Robot. Autom. Lett. 4 (2019) 1085–1092.
[38] A. Pretto, S. Aravecchia, W. Burgard, N. Chebrolu, C. Dornhege, T. Falck, F. Fleckenstein, A. Fontenla, M. Imperoli, R. Khanna, et al., Building an aerial–ground robotics system for precision farming: an adaptable solution, IEEE Robot. Autom. Mag. 28 (2020) 29–49.
[39] L. Quan, W. Jiang, H. Li, H. Li, Q. Wang, L. Chen, Intelligent intra-row robotic weeding system combining deep learning technology with a targeted weeding mode, Biosyst. Eng. 216 (2022) 13–31.
[40] M. Rienth, T. Scholasch, State-of-the-art of tools and methods to assess vine water status, Oeno One (2019).
[41] G. Ristorto, R. Gallo, A. Gasparetto, L. Scalera, R. Vidoni, F. Mazzetto, A mobile laboratory for orchard health status monitoring in precision farming, Chem. Eng. Trans. 58 (2017) 661–666.
[42] G. Rivera, R. Porras, R. Florencia, J.P. Sánchez-Solís, LiDAR applications in precision agriculture for cultivating crops: a review of recent advances, Comput. Electron. Agric. 207 (2023) 107737.
[43] R. Rossi, S. Costafreda-Aumedes, L. Leolini, C. Leolini, M. Bindi, M. Moriondo, Implementation of an algorithm for automated phenotyping through plant 3D-modeling: a practical application on the early detection of water stress, Comput. Electron. Agric. 197 (2022) 106937.
[44] R.B. Rusu, Z.C. Marton, N. Blodow, M. Dolha, M. Beetz, Towards 3D point cloud based object maps for household environments, Robot. Auton. Syst. 56 (2008) 927–941.
[45] V. Saiz-Rubio, F. Rovira-Más, A. Cuenca-Cuenca, F. Alves, Robotics-based vineyard water potential monitoring at high resolution, Comput. Electron. Agric. 187 (2021) 106311.
[46] P.F. Scholander, H. Hammel, E. Hemmingsen, E. Bradstreet, Hydrostatic pressure and osmotic potential in leaves of mangroves and some other plants, Proc. Natl. Acad. Sci. 52 (1964) 119–125.
[47] M.H. Siebers, E.J. Edwards, J.A. Jimenez-Berni, M.R. Thomas, M. Salim, R.R. Walker, Fast phenomics in vineyards: development of GRover, the grapevine rover, and LiDAR for assessing grapevine traits in the field, Sensors 18 (2018) 2924.
[48] A.C. Tagarakis, E. Filippou, D. Kalaitzidis, L. Benos, P. Busato, D. Bochtis, Proposing UGV and UAV systems for 3D mapping of orchard environments, Sensors 22 (2022) 1571.
[49] M. Tankari, C. Wang, H. Ma, X. Li, L. Li, R.K. Soothar, N. Cui, M. Zaman-Allah, W. Hao, F. Liu, et al., Drought priming improved water status, photosynthesis and water productivity of cowpea during post-anthesis drought stress, Agric. Water Manag. 245 (2021) 106565.
[50] J. Tardaguila, M. Stoll, S. Gutiérrez, T. Proffitt, M.P. Diago, Smart applications and digital technologies in viticulture: a review, Smart Agricult. Technol. 1 (2021) 100005.
[51] D. Tiozzo Fasiolo, L. Scalera, E. Maset, Comparing LiDAR and IMU-based SLAM approaches for 3D robotic mapping, Robotica (2023) 1–17.
[52] D. Tiozzo Fasiolo, L. Scalera, E. Maset, A. Gasparetto, Towards autonomous mapping in agriculture: a review of supportive technologies for ground robotics, Robot. Auton. Syst. 104514 (2023).
[53] S. Toscano, D. Scuderi, F. Giuffrida, D. Romano, Responses of mediterranean ornamental shrubs to drought stress and recovery, Sci. Hortic. 178 (2014) 145–153.
[54] C.C. Ulloa, A. Krus, A. Barrientos, J. del Cerro, C. Valero, Robotic fertilization in strip cropping using a CNN vegetables detection-characterization method, Comput. Electron. Agric. 193 (2022) 106684.
[55] C. Van Leeuwen, P. Darriet, The impact of climate change on viticulture and wine quality, J. Wine Econ. 11 (2016) 150–167.
[56] S. Vélez, M. Ariza-Sentís, J. Valente, Mapping the spatial variability of Botrytis bunch rot risk in vineyards using UAV multispectral imagery, Eur. J. Agron. 142 (2023) 126691.
[57] R. Vidoni, R. Gallo, G. Ristorto, G. Carabin, F. Mazzetto, L. Scalera, A. Gasparetto, ByeLab: an agricultural mobile robot prototype for proximal sensing and precision farming, in: ASME International Mechanical Engineering Congress and Exposition, American Society of Mechanical Engineers, 2017, p. V04AT05A057.
[58] F. Vulpi, R. Marani, A. Petitti, G. Reina, A. Milella, An RGB-D multi-view perspective for autonomous agricultural robots, Comput. Electron. Agric. 202 (2022) 107419.
[59] K. Wang, J. Zhou, W. Zhang, B. Zhang, Mobile LiDAR scanning system combined with canopy morphology extracting methods for tree crown parameters evaluation in orchards, Sensors 21 (2021) 339.
[60] L. Wang, Y. Miao, Y. Han, H. Li, M. Zhang, C. Peng, Extraction of 3D distribution of potato plant CWSI based on thermal infrared image and binocular stereovision system, Front. Plant Sci. 13 (2023) 1104390.
[61] M. Wichmann, M. Kamil, A. Frederiksen, S. Kotzur, M. Scherl, Long-term investigations of weather influence on direct time-of-flight lidar at 905 nm, IEEE Sens. J. 22 (2021) 2024–2036.
[62] P. Xie, R. Du, Z. Ma, H. Cen, Generating 3D multispectral point clouds of plants with fusion of snapshot spectral and RGB-D images, Plant Phenom. 5 (2023) 0040.
[63] J. Xue, B. Su, Significant remote sensing vegetation indices: a review of developments and applications, J. Sens. 2017 (2017).
[64] Z. Zhai, J.F. Martínez, V. Beltran, N.L. Martínez, Decision support systems for agriculture 4.0: survey and challenges, Comput. Electron. Agric. 170 (2020) 105256.
[65] C. Zhang, C. Mouton, J. Valente, L. Kooistra, R. van Ooteghem, D. de Hoog, P. van Dalfsen, P.F. de Jong, Automatic flower cluster estimation in apple orchards using aerial and ground based point clouds, Biosyst. Eng. 221 (2022) 164–180.
[66] W. Zhang, J. Qi, P. Wan, H. Wang, D. Xie, X. Wang, G. Yan, An easy-to-use airborne LiDAR data filtering method based on cloth simulation, Remote Sens. 8 (2016) 501.
[67] M. Zine-El-Abidine, H. Dutagaci, G. Galopin, D. Rousseau, Assigning apples to individual trees in dense orchards using 3D colour point clouds, Biosyst. Eng. 209 (2021) 30–52.